Closely Coupled Binary Metal Sulfide Nanosheets Shielded Molybdenum Sulfide Nanorod Hierarchical Structure via Eco-Benign Surface Exfoliation Strategy towards Efficient Lithium and Sodium-ion Batteries

Ganesh Kumar Veerasubramani [a], Myung-Soo Park [a], Hyun-Sik Woo [a], Yang-Kook Sun [b], Dong-Won Kim [a,c,*]

[a] *Department of Chemical Engineering, Hanyang University, Seoul 04763, Republic of Korea*
[b] *Department of Energy Engineering, Hanyang University, Seoul 04763, Republic of Korea*
[c] *Institute of Nano Science and Technology, Hanyang University, Seoul 04763, Republic of Korea*

A B S T R A C T

Improving interfacial interactions by constructing heterostructures is gaining interest due to its unique structural benefits for ion-reservoir applications. However, great challenges remain. Herein, we propose MoS_2 nanorod-based heterostructures covered with a closely interconnected Sn and Mo sulfides/carbon matrix (SMSC@MS-HS) (engraved by a simple water based surface exfoliation strategy) as an efficient anode material for Li/Na–ion storage. Our hierarchical SMSC@MS-HS electrode achieved remarkable discharge capacities of 1,060 and 490 mAh g^{-1} (after 100 cycles at 100 mA g^{-1}) for lithium and sodium-ion batteries, respectively, along with high initial coulombic efficiency and rate capability. This well-constructed architecture provided facile Li^+/Na^+ ion diffusion and enhanced the charge transfer at the heterointerfaces. Meanwhile, the strong coupling of MoS_2 with SnS during water exfoliation in the presence of a carbon matrix created a stable and shielded nanostructure, which significantly enhanced electron/ion transport and mitigated the volume expansion during cycling. These benefits were attributed to a prominent capacitive contribution from kinetics study, improved Li^+/Na^+ diffusion from galvanostatic intermittent titration measurements, and good structural stability from ex-situ analyses.

1. Introduction

Rechargeable batteries have received great attention over the last decade due to serious environmental problems and an increasing demand for energy storage devices [1,2]. Lithium-ion batteries (LIBs) have attracted much interest for their long-term stability, high voltage and high energy density compared to other energy storage systems [3-5]. Similarly, sodium-ion batteries (SIBs) are also good candidates because they have properties similar to LIB, but are cheaper and can be made from abundantly available materials [6-10]. Developing rechargeable LIBs/SIBs with exceptional energy density is of interest due to increasing demand for energy storage devices [11]. One strategy is to comprehend the fast and stable Li/Na-ion insertion/extraction upon continuous charging/discharging at the negative electrode. Various anode materials for LIBs/SIBs such as carbonaceous materials, transition metal oxides/sulfides/selenides and some metal alloys have been investigated extensively due to their high theoretical capacity [12-17]. Among them, transition metal sulfides consisting of an S-M-S bond structure (such as SnS_2, SnS, MoS_2) have drawn much attention

due to their high specific capacities and weak van der Waals forces, which are beneficial for Li/Na-ion diffusion with good reversibility for LIBs/SIBs [18,19]. For instance, MoS_2 has been actively studied as an anode material for LIBs/SIBs due to their widened interlayer spacing and ability to host the ions without large variation in volume. However, the poor intrinsic conductivity, cycling and rate capability limit the practical applicability of MoS_2 [20-22]. On the other hand, SnS is another promising anode material for LIBs/SIBs because the comparatively weak Sn-S bonds result in better coulombic efficiency and higher reversibility [23-25]. But, severe capacity fading of SnS by its large volume expansion upon continuous Li/Na-ion insertion/extraction causes aggregation and pulverization in the SnS electrode [26,27].

To overcome these issues, heterostructured materials have recently been developed by coupling two different metal sulfides/selenides that can improve the solid-electrolyte interface reaction kinetics and expedite charge transfer at the heterointerfaces [20,28-30]. Su et al. proposed a MoS_2/CoS_2 nanocomposite via interlayer confinement that enhances electrochemical kinetics for SIBs [31]. Liu et al. reported a $SnSe_2/ZnSe@PDA$ heterostructure that can provide fast reaction kinetics and good cycling behavior due to its lattice distortion and charge redistribution at the heterointerface junctions [32]. Man et al. reported that the interface response from layered metal sulfides of MoS_2/SnS_2 can provide longer layer distances in LIBs due to van der Waals

heterojunctions [33]. Cao et al. proposed that bimetallic Sb_2S_3/FeS_2 sulfide nanorods provide an enormous number of active sites at the interface of the heterojunction, thereby increasing the electrochemical kinetics as validated by in-situ and DFT measurements for sodium storage [34]. Recently, our group showed that the combination of $Fe_{1-x}S/MnS$ improves storage capability and reduces structural pulverization by co-operative effects in SIBs [35]. Hence, the rational design and appropriate synthesis of novel heterostructured materials with unique compositions and morphologies can greatly enhance the storage capability for various energy storage devices. However, big challenges still remain.

Creating porous structures like yolk-shell or hollow structures requires aggressive conditions such as high temperature treatment, acid etching, coating using some soluble materials in organic solvents or coating using polymers [32,36-38]. A novel strategy that does not use these severe conditions is needed for creating active electrode materials. Herein, we proposed a unique and simple water exfoliation strategy to create closely combined Sn and Mo sulfides with a carbon matrix over a MoS_2 nanorods hierarchical structure (SMSC@MS-HS) as an advanced material for Li/Na-ion storage. Developing this type of hierarchical electrode is to improve the capability of alleviating the volume change and facilitating Li^+/Na^+ transport by increasing the surface area and decreasing the diffusion length. The prepared SMSC@MS-HS electrodes delivered excellent rate capabilities of 752 mAh g^{-1} at 2000 mA g^{-1} for LIB, 420 mAh g^{-1} at 2000 mA g^{-1} for SIB, and good cycling stability with high initial coulombic efficiencies of 88.4% (LIB) and 90.5% (SIB). Ex-situ analyses revealed that such a hierarchical heterostructure could improve the electrochemical kinetics by promoting electron transfer at the junction and shielding the large volume variation during insertion/extraction of Li/Na ions.

2. Experimental Section

2.1. Synthesis of SnS/C@MoS$_2$ core-shell structure (SSC@MS-CS)

Initially, MoO_3 nanorods were prepared as described in our previous report [20]. Briefly, 200 mg of MoO_3 nanorods were dispersed together with $SnCl_4 \cdot 5H_2O$ and thioacetamide (1:1 weight ratio) along with a small amount of glucose in an ethylene glycol and ethanol mixture. The above solution was mixed well under magnetic stirring for a few hours. After achieving good dispersion, the solution was transferred to an autoclave vessel (Teflon lined). Then, the vessel was heated to 150°C for 6 hr. Greyish precipitate $SnS_x/C@MoO_3$ was collected, washed with a water/ethanol mixture using a refrigerated centrifuge, and dried at 80°C overnight. Finally, the collected powder was annealed at 500°C for 6 h with a sulfur powder under an argon/hydrogen (96/4%) atmosphere to obtain $SnS/C@MoS_2$ core-shell (SSC@MS-CS) powder.

2.2. Synthesis of SnS/MoS$_2$/C@MoS$_2$ hierarchical structure (SMSC@MS-HS)

The hierarchical structure of SMSC@MS-HS was prepared as follows. A small amount of $SnS_x/C@MoO_3$ core-shell material (achieved before sulfidation step) was dispersed into hot water (60°C preheated) and stirred mildly (200 rpm) for 30 min. After that, the solution was cooled down to room temperature immediately. Then, the collected precipitate was washed with ethanol and dried at 80°C overnight. Finally, the collected powder was annealed at 500°C for 6 h with sulfur powder inlet under an argon/hydrogen (96/4%) atmosphere to obtain SMSC@MS-HS. For comparison, pristine MoO_3 nanorods were directly sulfurized under the same conditions to produce pristine MoS_2 nanorods.

2.3. Structural Characterization

The morphologies and cross-sectional images of all the samples were investigated using FE-SEM (NOVA Nano SEM-450) integrated with energy dispersive spectroscopy (EDS) and HR-TEM equipped with ele-

mental mapping (JEOL JEM 2100F system) measurement. XRD patterns were obtained using a D8 Bruker XRD with Cu Kα radiation at a wavelength of 1.5405 Å in the 2θ range between 10 and 70º. Nitrogen adsorption/desorption isotherms were recorded using a Micromeritics TriStar II 3.02 version apparatus at 77 K. The powder samples were degassed at 200 °C for 2 h prior to the measurements. XPS spectra were obtained using a VG Multilab ESCA system: 220i).

2.4. Electrode Preparation and Electrochemical Characterization

To prepare working electrodes for MoS_2, SSC@MS-CS and SMSC@MS-HS, 70 wt.% of active materials were mixed with 15 wt.% Super P and 15 wt.% CMC in distilled water to make a homogeneous slurry. Then, it was coated onto the copper foil and dried under vacuum at 100°C for 12 h. The average mass loading was about 2.0 mg. CR2032-type coin cell was assembled in an argon filled glove box using the above electrodes against Na foil (Alfa Aesar) with a glass fiber separator (Whatman). Approximately 200 μl of 1 M $NaClO_4$ in ethylene carbonate/propylene carbonate (50:50 by volume) with 10 wt.% fluoroethylene carbonate (PANAX ETEC Co., Ltd.) was injected into the cell. Lithium and sodium-ion full cells were fabricated with NCM811 and NVP, respectively, using a SMSC@MS-HS anode. When assembling the full-cell, the N/P ratio was optimized to be 1.2. Prior to that, the cathode was prepared for half-cell test by mixing 80 wt.% NCM811 or NVP, 10 wt.% super P and 10 wt.% poly(vinylidene fluoride) (PVdF) binder using N-methyl-2-pyrrolidone (NMP). The slurry was coated onto the Al foil and dried under vacuum at 110 °C for 12 h. CV and EIS measurements were carried out using a CH instrument (CHI600D Electrochemical Workshop) at 25°C. The charge and discharge cycling test was performed using battery test equipment (WBCS 3000, WonA Tech Co., Ltd.) at 25°C.

3. Results and Discussion

The hierarchical structure of closely combined Sn and Mo sulfide shielded MoS_2 nanorods was designed and synthesized by a facile eco-friendly strategy, as graphically presented in Fig. 1. Briefly, MoO_3 NRs prepared via a hydrothermal approach were uniformly dispersed in ethylene glycol and an ethanol mixture. Subsequently, tin chloride (as a tin precursor), thioacetamide (as a sulfur precursor) and glucose (as a carbon precursor) were added and underwent hydrothermal treatment to produce a $SnS_x/C@MoO_3$ core-shell structure. Fig. S1 shows an X-ray diffraction (XRD) pattern of the as-prepared MoO_3. The diffraction pattern confirmed the formation of the orthorhombic phase of MoO_3 with a highly crystalline nature (matched with JCPDS no. 35-0609) [39]. In addition to the MoO_3 peaks from the XRD pattern of $SnS_x/C@MoO_3$ core-shell structure, a few additional broad peaks at angles of 17.4, 28.2, 50.0° could be also observed, indicating the formation of SnS_x along with MoO_3 without any other impurities (JCPDS: 23-0677), which belongs to the hexagonal phase of SnS_2 [40]. Fig. S2a-S2d show scanning electron microscopy (FE-SEM) images of the prepared pristine MoO_3, pristine MoS_2, SSC@MS-CS and SMSC@MS-HS nanostructures respectively, in which core-shell rods with coarse surfaces were observed in contrast to the smooth surfaces of pristine MoS_2 nanorods. This $SnS_x/C@MoO_3$ core-shell structure was turned into a $SnS_x/MoO_3/C@MoO_3$ hierarchical structure by a simple water exfoliation route. The surface of the core MoO_3 was etched using warm water due to its solubility. During exfoliation, some of the MoO_3 still persisted with the outer SnS_x/C, as shown in Fig. 1. Upon sulfurization reaction under a mixed gas atmosphere, this stranded MoO_3 with SnS_x/C shells, and inner MoO_3 nanorods reacted with the sulfur gas turning them into MoS_2. In contrast, outward facing SnS_x was reduced into SnS sheets. Typical TEM images of MoS_2 are displayed in Fig. 2a and 2b, revealing a smooth rod-shaped morphology with average sizes of 100 – 200 nm without any breaks even after a high temperature sulfurization reaction. Fig. 2c and 2d present TEM images of $SnS_x/C@MoS_2$ in which the

Fig. 1. Schematic presentation for the preparation of SMSC@MS-HS via hydrothermal and eco-friendly surface exfoliation strategy.
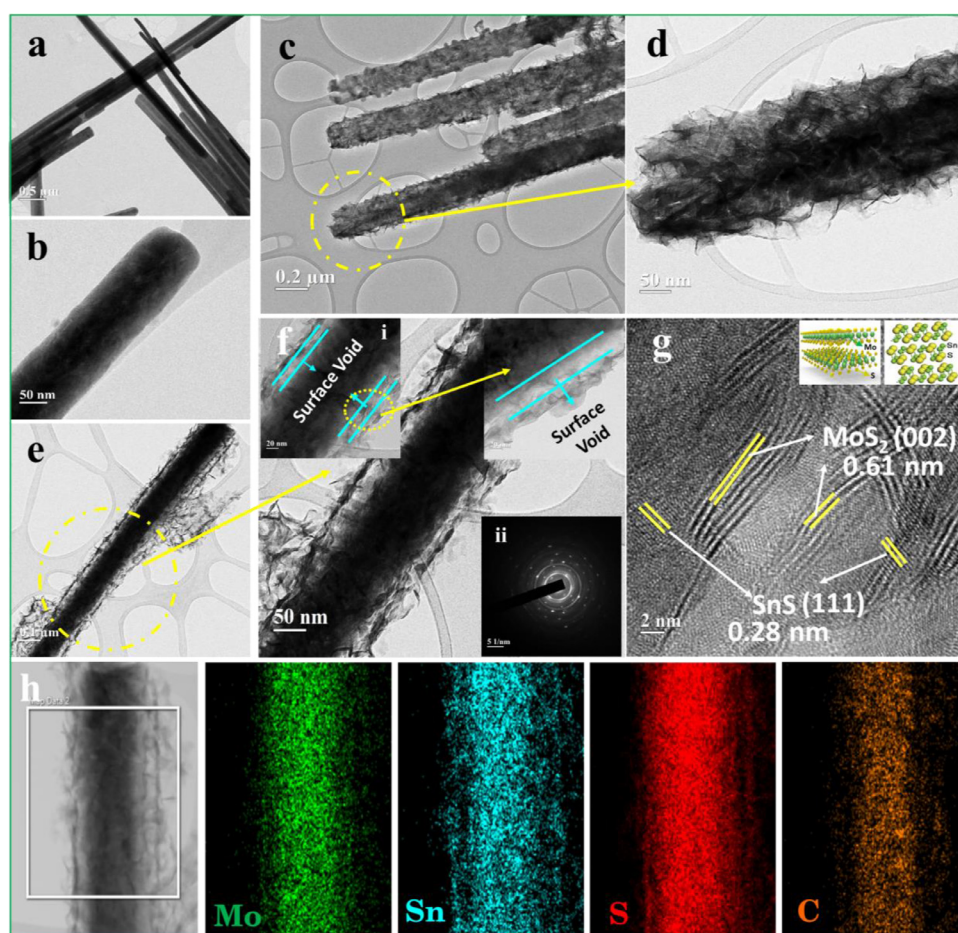

Fig. 2. TEM images of pristine MoS_2 at (a) low and (b) high magnification. (c) TEM images of SSC@MS-CS at (c) low and (d) high magnification. TEM images of SMSC@MS-HS at (e) low and (f) high magnification. Inset: (i) zoomed image showing the surface void between the MoS_2 core and SMSC shell, (ii) SAED pattern. (g) HR-TEM image of SMSC@MS-HS, (h) EDS mapping of Mo, Sn, S and C for SMSC@MS-HS.

small sheet-like morphology of SnS_x/C was uniformly achieved throughout the MoS_2 nanorods. The corresponding HR-TEM images before and after sulfidation reaction are shown in Fig. S3, in which two different interlayers belonging to (001) and (100) could be observed for SnS_2 before sulfidation, whereas (120) and (021) planes of SnS after sulfidation [40]. The EDS mapping images are presented in Fig. S4, suggesting the presence of uniformly distributed Mo, Sn, S and C in SSC@MS-CS. After exfoliation treatment, a tiny void was created between the inner MoS_2 nanorods and outer SMSC shell, as displayed in Fig. 2e and 2f. The inset of Fig. 2f (i) shows the enlarged images in which void spaces are apparent. The corresponding selected area diffraction (SAED) pattern (inset of Fig. 2f (ii)) reveals the coexistence of both SnS and MoS_2 as confirmed

by the respective crystalline and polycrystalline natures. Fig. 2g shows HR-TEM images of the SMSC@MS-HS, which presented well-structured lattice fringes. Two major interlayer spacings of 0.61 and 0.28 nm were apparently attributed to the MoS_2 (002) and SnS (111) planes with a carbon matrix. The corresponding elemental mapping results in Fig. 2h confirmed that the Sn, Mo, Sn and C signals were distributed around the MoS_2 nanorods, confirming the uniform distribution and complete coverage of SMSC sheets on the surface of MoS_2 nanorods with obvious nanovoids.

XRD measurements were performed to determine the phase composition and crystal structure, and the results are presented in Fig. 3a. The peaks were indexed to the composition of orthorhombic type SnS
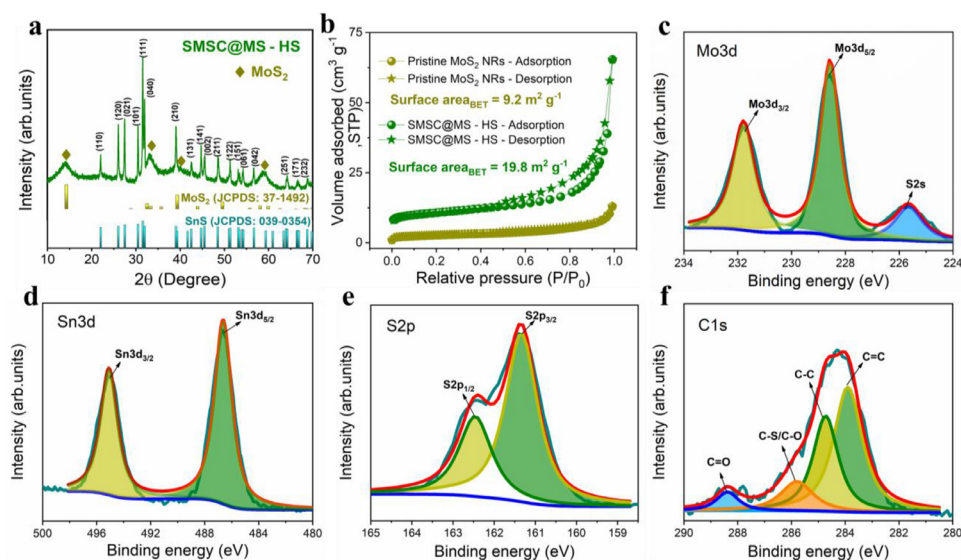
Fig. 3. (a) XRD pattern, (b) N_2 adsorption/desorption isotherm and (c)-(e) XPS spectra of SMSC@MS-HS. (c) Mo3d core-level, (d) Sn3d core-level, (e) S2p core-level and (f) C1s core level spectra.

(JCPDS: 039-0354) and hexagonal type MoS_2 (JCPDS: 37-1492) without any impurity peaks. Specific surface area of bare MoS_2 NRs and SMSC@MS-HS samples were calculated using BET (Brunauer–Emmett–Teller) measurements, as presented in Fig. 3b. SMSC@MS-HS had a large specific surface area of 19.8 m^2 g^{-1} due to the coarsened structure and ultrathin NSs. Pristine MoS_2 NRs exhibited a value of only 9.2 m^2 g^{-1}, which is two-fold lower than SMSC@MS-HS. Such an improved surface area will enhance host ion transport and alleviate the volume strain of inner MoS_2 NRs upon cycling. X-ray photoelectron spectroscopy (XPS) was also investigated to probe state of chemical bonding and state of valence in the SMSC@MS-HS sample. Fig. 3c displays the XPS core-level spectrum of Mo3d, and the peaks were centered at 228.6 eV for $Mo3d_{5/2}$, 231.8 eV for $Mo3d_{3/2}$ core-levels. In addition, the S2s peak was identified at a binding energy of 225.7 eV [41]. Fig. 3d shows the Sn3d core-level spectrum. A couple of peaks could be observed at 486.7 and 495.2 eV, corresponding to $Sn3d_{5/2}$ and $Sn3d_{3/2}$ respectively [42]. As can be seen in Fig. 3e, the S2p core-level also exhibits a pair of peaks centered at 161.3 and 162.5 eV, corresponding to $S2p_{3/2}$ and $S2p_{1/2}$, respectively. The results confirmed that the carbon layers were bonded to MoS_2 and SnS by C-S covalent bonds, as confirmed by the C1s core-level spectrum (Fig. 3f) [43]. Two major peaks identified at binding energies of 283.9 and 284.7 eV were associated with C=C and C-C bonds, respectively. Further, a pair of minor peaks could be observed at 285.8 and 288.4 eV, which corresponded to C-S/C-O and C=O, respectively. Subsequently, the upward shift of the C1s core-level peaks indicates that the electron cloud bias around the MoS_2 and SnS was due to the carbon atoms [44,45]. Compared to standard peaks, Sn3d, Mo3d and S2p core-level peaks in SMSC@MS-HS were shifted towards lower binding energies, signifying the rich electron cloud density around the MoS_2 NRs [45]. The strong coupling and improved interactions between SnS and MoS_2 due to the electron cloud bias from SnS to MoS_2 further confirmed the formation of a nanosized heterojunction between SnS and MoS_2. The intimate connections caused by SMS and C are likely key in preserving SMS, reaction products and providing improved electronic conduction upon cycling [46,47].

To elucidate the lithium storage ability in the prepared materials, cyclic voltammetry, charge- discharge and electrochemical impedance analyses were performed. Fig. 4a presents CV curves between 3.0 and 0.01 V at 0.1 mV s^{-1}. During the first cathodic scan, the peak observed at 1.0 V corresponded to the decomposition of SnS into Sn and Li_2S. A peak at around 0.5 V was attributed to the conversion process of MoS_2 with Na to form Na_xMoS_2, a solid electrolyte interphase (SEI), while the Li_xSn alloying process was observed in a broad peak below 0.25 V [48]. From

the second cathodic scan, the peak at 1.96 V corresponded to the reduction of sulfur into Li_2S. In addition, a pair of peaks between 1.0 to 1.5 V could be observed, which were assigned to the reactions of SnS to Sn and MoS_2 to Mo [20,48]. Turning to the first anodic scan, the peak at around 0.6 V can be ascribed to the delithiation of Li_xSn to Li^+. Two more peaks around 1.9 and 2.25 V were also observed in the high potential region. These peaks were related with the oxidation reaction of metallic Sn with Li_2S and metallic Mo with Li_2S, respectively [49,50]. They were very similar to the second anodic scan. Fig. 4b displays the typical charge and discharge curves of the SMSC@MS-HS electrode. As shown in figure, the initial charge and discharge capacities of the SMSC@MS-HS electrode were 996 and 881 mAh g^{-1} with an initial coulombic efficiency (ICE) of 88.4% at 50 mA g^{-1}. ICE values of 83.9 and 85.3% were obtained for pristine MoS_2 NRs and SSC@MS-CS electrodes, respectively (Fig. S5). For comparison, the electrochemical performance of pristine SnS, MoO_3 and SnS_2@MoO_3 before sulfidation reaction for LIB is presented in Fig. S6, S7 and S8, respectively. They revealed that cycling performance of these pristine samples was inferior to that of the SMSC@MS-HS electrode in terms of discharge capacity and cycling stability. Fig. 4c presents a comparison of the ICE of the SMSC@MS-HS heterostructured electrode and recent literature on Sn and Mo based sulfides for LIBs. Generally, the loss of initial capacity depends on the irreversible reaction of the electrode during charge and discharge, the irreversible decomposition of electrolytes, trapping due to defects or functional groups and other side reactions. The prepared SMSC@MS-HS heterostructured electrode provided improved reaction kinetics, ion insertion/extraction reversibility, ion diffusion paths and a stable SEI layer. Thus, significant improvement in the ICE could be achieved. As shown in Fig. 4d, the specific capacity of SSC@MS-CS and SMSC@MS-HS increased upon cycling up to 80 cycles due to the activation process, and steady state was subsequently achieved. After 100 cycles, maximum discharge capacities of 966 and 1060 mAh g^{-1} were achieved for SSC@MS-CS and SMSC@MS-HS, respectively, whereas drastic capacity fading was observed for pristine MoS_2 NRs before 50 cycles. In the course of the cycles, SMSC@MS-HS showed stable coulombic efficiencies up to 100%. In contrast, pristine MoS_2 NRs showed reduced coulombic efficiency as capacity fades. Similarly, the rate capabilities of the prepared electrodes (Fig. 4e) were investigated at different current densities ranging from 50 to 2000 mA g^{-1}. The SMSC@MS-HS electrode delivered excellent discharge capacities, especially at high current (752 mAh g^{-1} at 2000 mA g^{-1}), that is, 80% with respect to the capacity obtained at 50 mA g^{-1}. Electrochemical impedance spectroscopy (EIS) was performed, and the results are presented as a Nyquist plot in Fig. 4f. An equivalent circuit
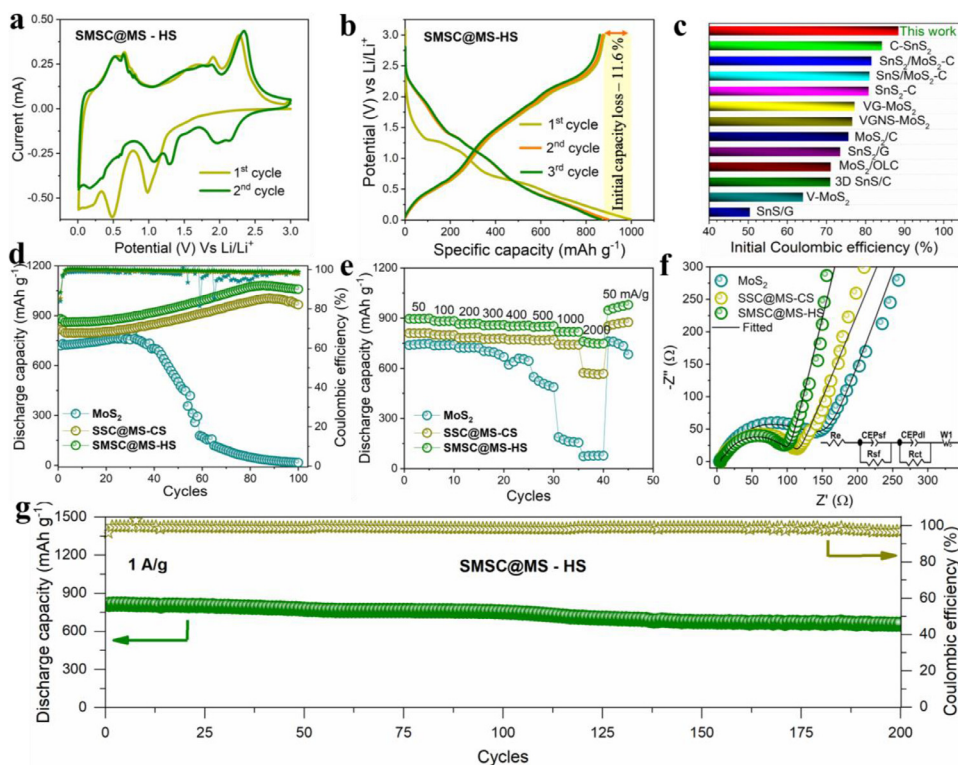
Fig. 4. LIB performance: (a) Cyclic voltammetry curves of SMSC@MS-HS, (b) charge and discharge curves of SMSC@MS-HS, (c) ICE comparison of Sn and Mo sulfide-based LIBs and SMSC@MS-HS in this work, (d) cycling stability at 100 mA g^{-1}, (e) rate capability at various current densities, (f) EIS Nyquist plot for pristine MoS$_2$ NRs, SSC@MS-CS and SMSC@MS-HS electrodes, (g) cycling stability at 1 A g^{-1} for SMSC@MS-HS electrode.

to fit the experimental data is given in the inset of figure. Each spectrum showed overlapped semicircles at the high and intermediate frequency regions, which are corresponding to lithium-ion diffusion through SEI layer and charge transfer process, respectively. The intercept on the real axis at high frequency is corresponding to the electrolyte resistance. The straight line at the low frequency region was associated with the Warburg impedance. As shown in the plot, the broadness of the semicircle at the high and medium frequency zone was reduced in the plot for the SMSC@MS-HS electrode compared with that for the SSC@MS-CS and pristine MoS$_2$ electrodes, signifying reduced charge transfer resistance (R$_{ct}$) at the interface of electrode-electrolyte. This result can be ascribed to the strong binding and the presence of SMSC on the outer shell. As a result, the improved charge-transfer characteristics in the SMSC@MS-HS could significantly enhance the storage ability. Further, a high discharge capacity of 655 mAh g^{-1} was retained after 200 cycles at 1000 mA g^{-1} (Fig. 4g). Overall electrochemical performance of SMSC@MS-HS electrode was compared with recent reports on metal sulfides for LIBs in Table S1. Such an excellent cycling stability at high current density was related to the hierarchical structure design in which the available void space can effectively accommodate the volume strain created over the inner MoS$_2$ NRs upon Li-ion insertion, mitigating structural pulverization of the electrode materials. The ternary SMSC shells also provide generous electrode/electrolyte contact areas that improve the conductivity and shorten the Li$^+$ diffusion and electron pathways upon cycling, thus boosting the high rate cycling performance.

Sodium storage performance of the SMSC@MS-HS electrode was evaluated between 3.0 - 0.01 V at 0.1 mV s^{-1}, as presented in Fig. 5a. As shown, the broad peak around 0.61 V might be due to the alloying reaction of Na/Sn, the conversion reaction of Na$^+$ ions with MoS$_2$ interlayers to form Na$_x$MoS$_2$ and SEI layer formation during the 1st cathodic scan [51]. The peak below 0.2 V might be associated with the conversion reaction of Na$_x$MoS$_2$ to Na$_2$S and Mo [52]. From the second cathodic scan, one more peak at 1.0 V was observed, indicating the SnS to Sn conversion, whereas a mild peak shifting to 0.63 from 0.61 V in the first scan might be correlated with the multistep Sn alloying reaction where

sodium ions form Na$_x$Sn and MoS$_2$ to Na$_x$MoS$_2$ [53-55]. During the first anodic scan, two peaks at 0.73 and 1.14 V can be related to dealloying of Na$_x$Sn to Sn and the Na$_2$S/Sn to SnS reverse conversion reaction, respectively [54,55]. A peak at 1.78 V was associated with the oxidation of Mo to MoS$_2$ [53,55,56]. Charge and discharge cycling test of the SMSC@MS-HS electrode was performed against Na metal in the half-cell configuration, similar to the LIB. Fig. 5b displays the voltage profiles of the SMSC@MS-HS electrode for the first three cycles consisting of two formation cycles at 50 mAg^{-1} and the first cycle at 100 mA g^{-1}. As presented, the initial charge and discharge capacities of SMSC@MS-HS electrode were 617 and 559 mAh g^{-1} at 50 mA g^{-1} with a high ICE of 90.6%. On the other hand, ICE values of only 85.8 and 87.4% were obtained for pristine MoS$_2$ NRs and SSC@MS-CS electrodes, respectively (Fig. S9). For comparison, the electrochemical performance of pristine SnS, MoO$_3$ and SnS$_2$@MoO$_3$ before sulfidation reaction for SIB is presented in Fig. S10, S11 and S12, respectively. Similar to the LIB, the initial and successive discharge capacities were deprived, suggesting the low reversible capacity and poor cycling stability for pristine samples. Fig. 5c presents the ICE comparison of the SMSC@MS-HS heterostructured electrode and recent literature on Sn and Mo-based sulfides for SIBs. Like the LIBs, the prepared SMSC@MS-HS heterostructured electrode exhibited high ICE compared to most of the Sn and Mo-based sulfides. Fig. 5d demonstrates the cycling stability comparison of pristine MoS$_2$ NRs, SSC@MS-CS and SMSC@MS-HS at 100 mA g^{-1}. As shown in the figure, the specific capacities of SSC@MS-CS and SMSC@MS-HS electrodes were stable with a slight increase upon cycling up to 80 cycles, then a slight drop thereafter. After 100 cycles, maximum discharge capacities of 364.8 and 487.8 mAh g^{-1} were achieved for SSC@MS-CS and SMSC@MS-HS, respectively, whereas a gradual decrease in capacity was observed from initial cycles for pristine MoS$_2$ NRs (~55% capacity retention). Similarly, rate capabilities of the prepared electrode materials (Fig. 5e) were measured from 50 to 2000 mA g^{-1}. The SMSC@MS-HS electrode delivered excellent discharge capacities especially at high current density (~420 mAh g^{-1} at 2000 mA g^{-1}). Like LIB, the diameter of the semicircle at the high and medium frequency region was decreased
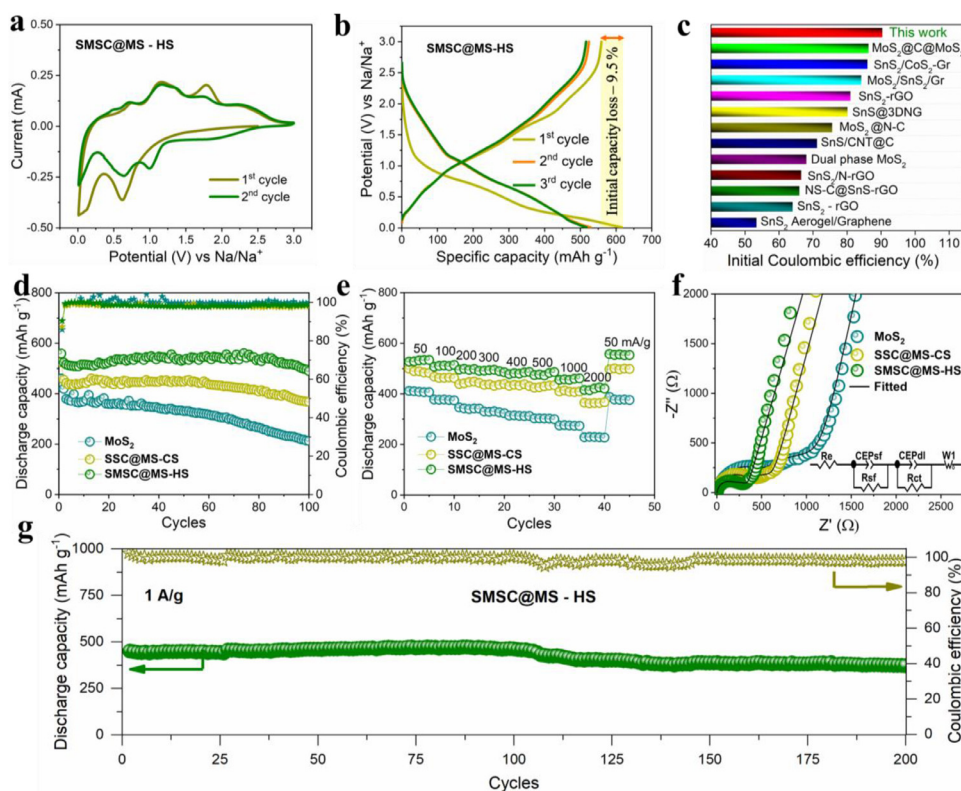
Fig. 5. SIB performance: (a) cyclic voltammetry curves of SMSC@MS-HS, (b) charge and discharge curves of SMSC@MS-HS, (c) ICE comparison of Sn and Mo sulfide-based SIBs and SMSC@MS-HS in this work, (d) cycling stability at 100 mA g^{-1}, (e) rate capability at various current densities, (f) EIS Nyquist plot for pristine MoS$_2$ NRs, SSC@MS-CS and SMSC@MS-HS electrodes, (g) cycling stability at 1 A g^{-1} for SMSC@MS-HS electrode.

for the SMSC@MS-HS electrode compared with the SSC@MS-CS and pristine MoS$_2$ electrodes, indicating enhanced charge transfer characteristics in the SMSC@MS-HS, which might be the reason for the improved sodium storage ability. In addition, a relatively high discharge capacity of 371 mAh g^{-1} was achieved after 200 cycles at 1000 mA g^{-1} (Fig. 5g). The overall performance of SMSC@MS-HS electrode was compared with recent literature based on metal sulfides for SIBs in Table S2.

Kinetic analyses such as the galvanostatic intermittent titration technique (GITT) and CV measurement at different scan rates were carried out for both LIB and SIB to estimate the Li/Na diffusion coefficient and capacitive contribution, respectively. Fig. 6a and 6c present the GITT curves at 100 mA g^{-1} after a pair of formation cycles for LIB and SIB, respectively. Both curves showed multi-step lithiation/delithiation and sodiation/desodiation reactions of SMSC@MS-HS on ion-diffusion. The increased lithiation and de-sodiation parts and corresponding diffusion coefficients are shown in Fig. 6b. As presented in figure, the diffusion coefficients were almost the same at the selected zone. The higher Li$^+$/Na$^+$ diffusion coefficient of the SMSC@MS-HS electrode was ascribed to the nano-crystalline zones, which reduced the diffusion length of the solid-phase. Although the Li$^+$/Na$^+$ diffusion coefficient in SMSC@MS-HS changed slightly, it remained almost steady at the selected regions and higher than that of single metal sulfides, implying that the bimetallic sulfides provided an improvement in ion diffusion [57]. This fast Li/Na ion diffusion can be explained as follows. First, phase boundaries could hinder the development of crystalline domains and build active sites and crystal defects. Secondly, out-of-step reactions and various redox potentials of two phase binary metal sulfides can alleviate the stress upon cycling. The electrochemical kinetics of the SMSC@MS-HS heterostructured electrode was further investigated by cyclic voltammetry at various sweep rates ranging from 0.1 to 1.0 mV s^{-1}. These results are presented in Fig. 6d and 6g for LIB and SIB, respectively. As shown in both figures, the CV curves were well maintained from low to high scan rates, suggesting good reversible behavior of the electrodes. Contributions from capacitive and diffusion currents could be measured using the relation i = k$_1\nu$ + k$_2\nu^{1/2}$ (ν is scan rate, k$_1\nu$ is capacitive contribution,

k$_2\nu^{1/2}$ is diffusion contribution) [58]. Differences between the capacitive and diffusion contributions of the CV curves are shown in Fig. 6e and 6h for LIB and SIB, respectively. The corresponding contributions at the various scan rates are also presented in Fig. 6f and 6i. According to the calculations, maximum capacitive contributions achieved for LIB and SIB at 1 mV s^{-1} were 83.2 and 80.4%, respectively. The influence of capacitive contribution of the SMSC@MS-HS heterostructured electrode to the total capacity was attributed to the fast electrochemical kinetics.

Postmortem analysis is an important procedure in energy storage devices to understand the physical and chemical interactions that are present during charging/discharging at the interface of an electrode and electrolyte. Fig. 7 shows an ex-situ analysis for pristine MoS$_2$ NRs and SMSC@MS-HS electrodes after 100 cycles for LIB. As shown in Fig. 7a (i), a brown solution was observed within a few minutes of sonication for pristine MoS$_2$ NRs after cycling, indicating the loss of binding ability from the current collector. On the other hand, no dissolution was observed for the SMSC@MS-HS electrode even after more cycles, clearly revealing the excellent binding ability of the SMSC@MS-HS to the current collector (Fig. 7b (i)). TEM and XRD measurements were performed for both electrodes after cycling. As shown in the ex-situ TEM images in Fig. 7a (ii), the rod shaped morphology of MoS$_2$ was fully damaged due to its large volume expansion upon continuous cycles. On the other hand, the rod-shaped morphology of the SMSC@MS-HS electrode was almost maintained by hierarchical outer ternary SMSC shells (Fig. 7b (ii)). The measured interlayer spacing for the SMSC@MS-HS electrode in HR-TEM indicates the presence of a (111) plane for SnS. The ex-situ XRD patterns for the pristine MoS$_2$ and SMSC@MS-HS electrodes are presented in Fig. 7b (iii). Clearly, the high intensity peaks of MoS$_2$ around 14° (which is responsible for the high interlayer distance of MoS$_2$) totally disappeared except for the broad peak between 35-45°, indicating that an amorphous phase was formed after cycling. Similarly, no peaks could be observed for MoS$_2$, except a few peaks for SnS (♣) and Sn in the SMSC@MS-HS electrode after cycling. This observation agreed well with the ex-situ HR-TEM measurement. In addition, two high intensity peaks were identified for Cu substrates. Based on the ex-situ results,
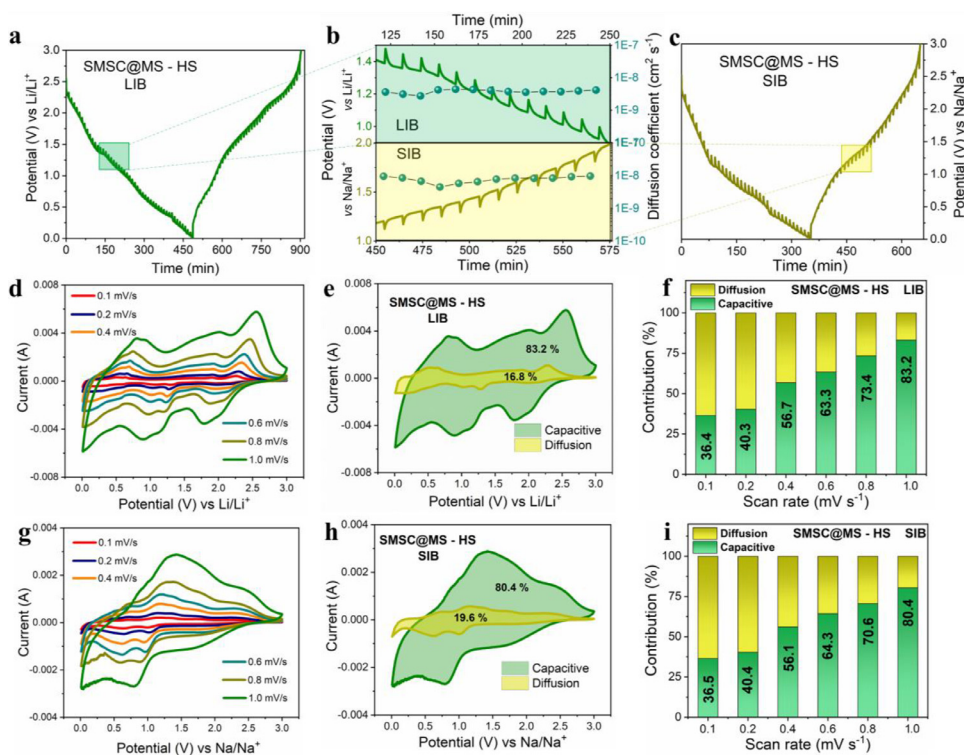
Fig. 6. Kinetic study of SMSC@MS-HS electrode: GITT curves for (a) LIBs, (c) SIBs and (b) corresponding diffusion coefficient in the marked region. (d) CV curves at various scan rates ranging from 0.1 – 1.0 mV s^{-1} in LIB. (e) Diffusion and capacitive separation curve at 1 mV s^{-1} in LIB, (f) contribution percentage of diffusion and capacitive controlled reaction at various scan rates in LIB. (g) CV curves at various scan rates ranging from 0.1 – 1.0 mV s^{-1} in SIB. (h) Diffusion and capacitive separation curve at 1 mV s^{-1} in SIB, (i) contribution percentage of diffusion and capacitive controlled reaction at various scan rates in SIB.
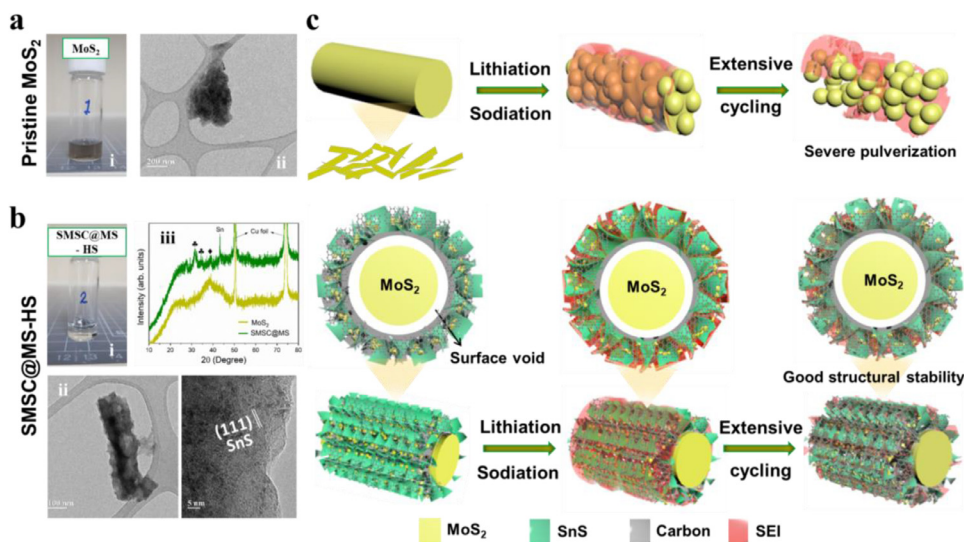

Fig. 7. (a) Photographic image of pristine MoS$_2$ NRs after bath sonication cycles for 15 min and TEM image of pristine MoS$_2$ NRs after cycles. (b) Photographic image of pristine MoS$_2$ NRs after bath sonication cycles for 15 min, XRD pattern, TEM and HR-TEM images. (c) A schematic representation of the effect of structural pulverization upon continuous cycling for pristine MoS$_2$ NRs and SMSC@MS-HS electrodes.

schematics can be drawn in Fig. 7c for both lithiation and sodiation upon extensive cycling to illustrate the advantages of the SMSC@MS-HS heterostructure. Fig. S13 and S14 present a comparison of Nyquist plots before and after cycling at 100 mAg^{-1}. Therein, the lower concaved semicircle for pristine MoS$_2$ in both LIB/SIB (Fig. S13a and S14a) signifies an increase in R$_{ct}$. This might be due to the loss of contact between neighboring nanorods and active materials from the current collector in pristine MoS$_2$ electrode. In contrast, this phenomenon was controlled in the SMSC@MS-HS electrode, as shown in Fig. S13b and S14b for both LIB and SIB. To further elucidate the enhanced stability of SMSC@MS-HS, ex-situ cross-sectional FE-SEM images were obtained after cycles with comparison of pristine MoS$_2$ electrode (Fig. S15a and S15b). As expected, the excellent adhesion was observed in SMSC@MS-HS electrode compared to pristine MoS$_2$ electrode after continuous charge and

discharge cycles. The overall ex-situ analyses confirmed the efficient binding of the SMSC@MS-HS electrode after cycling. The presence of hierarchical outer ternary SMSC shells in SMSC@MS-HS effectively alleviated the volume expansion upon continuous lithiation/sodiation cycles.

To elucidate the practical applications of the SMSC@MS-HS electrodes, full cells were assembled using LiNi$_{0.8}$Co$_{0.1}$Mn$_{0.1}$O$_2$ (NCM811) and Na$_3$V$_2$(PO$_4$)$_3$ (NVP) for LIB and SIB, respectively, as displayed in Fig. 8a. Prior to assembling the full cell, half-cell performance of NCM811 (Fig. S16) and NVP (Fig. S17) was evaluated. As shown in figures, remarkable discharge capacities of 194.5 and 105.0 mAh g^{-1} were achieved for NCM811 and NVP electrodes, respectively, with good cycling stability. Fig. 8b and 8c compare the charge-discharge curves for anodes, cathodes and full cells for LIB and SIB, respectively. Fig. 8d and
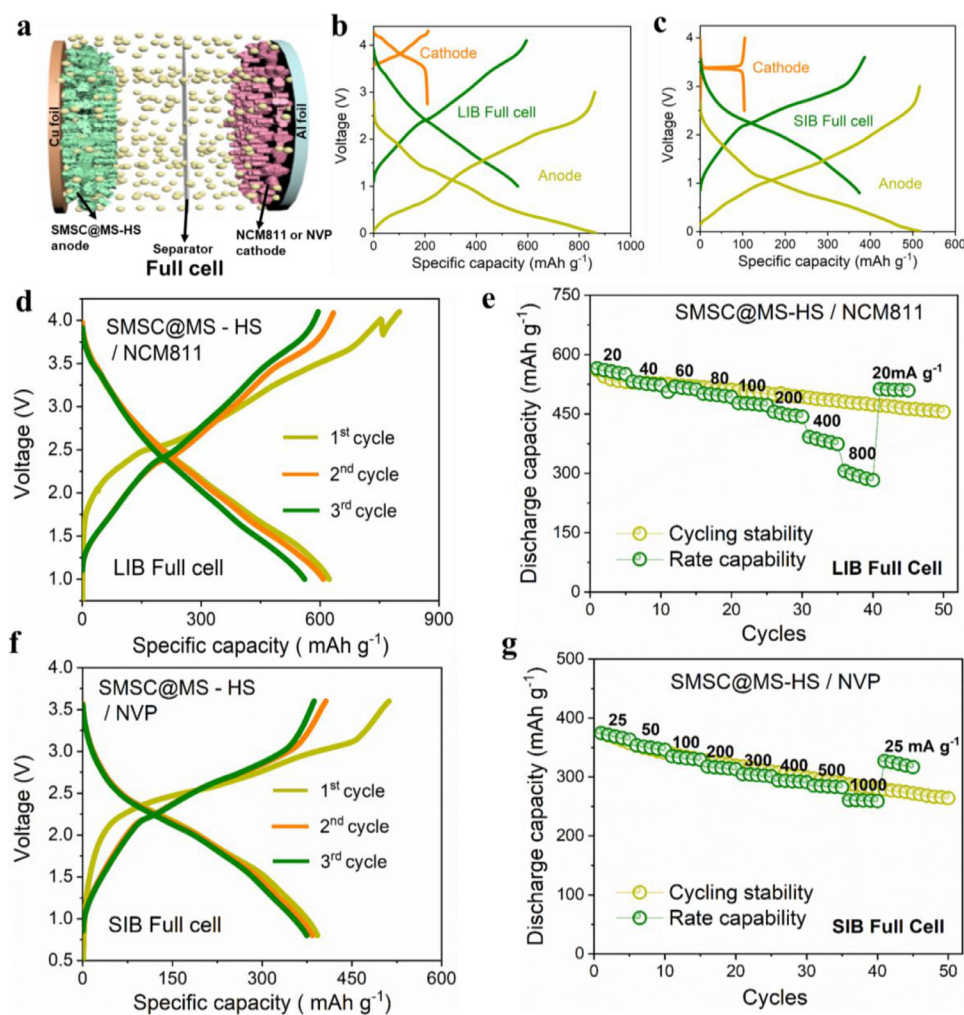
Fig. 8. (a) Schematic illustration of full cell fabrication consisting of SMSC@MS-HS anode and NCM811 or NVP cathode. Comparison of charge-discharge curves of cathode, anode and full cell for (b) LIB and (c) SIB. (d) Charge and discharge curves of assembled LIB, (e) cycle and rate performance of assembled LIB full cell, (f) charge and discharge curves of assembled SIB, (g) cycle and rate performance of assembled SIB full cell. (Note that the specific capacities of full cells were calculated based on anode mass).

8f show the charge-discharge curves for SMSC@MS-HS/NCM811 and SMSC@MS-HS/NVP full cells in the voltage ranges between 1.0 - 4.1 and 0.8 - 3.6 V, respectively. Maximum discharge capacities of 623.0 and 392.5 mAh g^{-1} (based on anode weight) were obtained for LIB and SIB full cells, respectively. After formation cycles, all the curves were almost overlapped each other, showing very good cycling stability. Fig. 8e and 8g present the cycling stability and rate capability at different current rates. Both SMSC@MS-HS/NCM811 and SMSC@MS-HS/NVP full cells exhibited an excellent cycling stability and rate capability. Discharge capacities of 455 and 264 mAh g^{-1} were achieved at the end of 50 continuous cycles for SMSC@MS-HS/NCM811 and SMSC@MS-HS/NVP full cells, respectively. These results demonstrate that SMSC@MS-HS can be used as a promising anode material for Li and Na-ion storage applications.

4. Conclusion

In summary, we demonstrated the synthesis of SMSC shielded MoS$_2$ nanorods with adequate surface voids by a simple, hydrothermal, eco-benign water exfoliation method followed by annealing treatments. The simple water exfoliation strategy to create pores over the surface of inner core materials had an enormous benefit compared to vigorous commercial treatments. This internal void space in the prepared SMSC@MS-HS accommodated volume expansion during repeated charge and discharge cycles. The generous phase boundaries of the bi-metallic sulfides on the outer shell promoted the electronic/ionic conductivity, and an enhancement in the reversibility was achieved during lithiation/sodiation. Furthermore, SMSC@MS-HS provided an excellent pseudocapacitive contribution, and increased diffusion coefficients were responsible for the excellent rate and cycling performance. Post-mortem analysis showed that the improved Li/Na storage performance was achieved by the hierarchical outer ternary SMSC shells in SMSC@MS-HS. As a result, the SMSC@MS-HS heterostructured electrode exhibited outstanding cycling performance in both LIB and SIB full cells. Based on the measured electrochemical performance, the SMSC@MS-HS is a promising anode material for energy storage applications.

Declaration of Competing Interest

The authors declare no conflict of interest.

CRediT authorship contribution statement

Ganesh Kumar Veerasubramani: Conceptualization, Methodology, Investigation, Data curation, Writing - original draft. **Myung-Soo Park:** Formal analysis, Investigation. **Hyun-Sik Woo:** Formal analysis, Investigation. **Yang-Kook Sun:** Visualization, Supervision, Writing - review & editing. **Dong-Won Kim:** Supervision, Writing - review & editing, Project administration, Funding acquisition.

Acknowledgements

ICT and Future Planning) (No. 2019R1A4A2001527) and the research fund of Hanyang University (HY-2020). GKV would like to thank Dr. Goli Nagaraju for his valuable inputs on schematics for this work.

Supplementary materials

Supplementary material associated with this article can be found, in the online version, at doi:10.1016/j.ensm.2021.03.022.

References

[1] L. Schlapbach, A. Züttel, Hydrogen-storage materials for mobile applications, Nature 414 (2001) 353–358.

[2] Y. Kim, J. Koh, Q. Xie, Y. Wang, N. Chang, M. Pedram, A scalable and flexible hybrid energy storage system design and implementation, J. Power Sources 255 (2014) 410–422.

[3] B. Scrosati, J. Garche, Lithium batteries: Status, prospects and future, J. Power Sources 195 (2010) 2419–2430.

[4] B. Dunn, H. Kamath, J.M. Tarascon, Electrical energy storage for the grid: A Battery of Choices, Science 334 (2011) 928–935.

[5] M. Armand, J.M. Tarascon, Building better batteries, Nature 451 (2008) 652–657.

[6] J.-W. Choi, D. Aurbach, Promise and reality of post-lithium-ion batteries with high energy densities, Nat. Rev. Mater. 1 (2016) 16013.

[7] Y. Naoaki, K. Kei, D. Mouad, K. Shinichi, Research development on sodium-ion batteries, Chem. Rev. 114 (2014) 11636–11682.

[8] H.-S. Kim, H.-G. Kim, Z. Ding, M.-H. Lee, K.-M. Lim, G. Yoon, K.-S. Kang, Recent progress in electrode materials for sodium-ion batteries, Adv. Energy Mater. 6 (2016) 1–38 1600943.

[9] D. Yang, Y. Zhou, H. Geng, C. Liu, B. Lu, X. Rui, Q. Yan, Pathways towards high energy aqueous rechargeable batteries, Coord. Chem. Rev. 424 (2020) 213521.

[10] X. Rui, X. Zhang, S. Xu, H. Tan, Y. Jiang, L.Y. Gan, Y. Feng, C.C. Li, Y. Yu, A low-temperature sodium-ion full battery: Superb kinetics and cycling stability, Adv. Funct. Mater. 31 (2020) 2009458.

[11] C.Y. Yu, J.S. Park, H.G. Jung, K.Y. Chung, D. Aurbach, Y.K. Sun, S.T. Myung, NaCrO$_2$ cathode for high-rate sodium-ion batteries, Energy Environ. Sci. 8 (2015) 2019–2026.

[12] Y. Subramanian, G.K. Veerasubramani, M.-S. Park, D.-W. Kim, Investigation of layer structured NbSe2 as an intercalation anode material for sodium-ion hybrid capacitors, J. Electrochem. Soc. 166 (2019) A598–A604.

[13] T. Zhou, W.-K. Pang, C. Zhang, J. Yang, Z. Chen, H.-K. Liu, Z. Guo, Enhanced sodium-ion battery performance by structural phase transition from two-dimensional hexagonal-SnS$_2$ to orthorhombic-SnS, ACS Nano 8 (2014) 8323–8333.

[14] J.-Y. Hwang, S.-T. Myung, Y.-K. Sun, Sodium-ion batteries: present and future, Chem. Soc. Rev. 46 (2017) 3529–3614.

[15] W. Qi, J.G. Shapter, Q. Wu, T. Yin, G. Gao, D. Cui, Nanostructured anode materials for lithium-ion batteries: principle, recent progress and future perspectives, J. Mater. Chem. A 5 (2017) 19521–19540.

[16] H. Tan, Y. Feng, X. Rui, Y. Yu, S. Huang, Metal chalcogenides: Paving the way for high-performance sodium/potassium-ion batteries, Small Methods 4 (2020) 1900563.

[17] S. Zhang, H. Tan, X. Rui, Y. Yu, Vanadium based materials: Next generation electrodes powering the battery revolutions? Acc. Chem. Res. 53 (2020) 1660–1671.

[18] Y. Lim, X. Guo, M. Hu, B. Liu, Y. Dong, X. Wang, N. Li, H.E. Wang, A MoS$_2$@SnS heterostructure for sodium-ion storage with enhanced kinetics, Nanoscale 12 (2020) 1468–14698.

[19] L. Mei, C. Xu, T. Yang, J. Ma, L. Chen, Q. Li, T. Wang, Superior electrochemical performance of ultrasmall SnS$_2$nanocrystals decorated on flexible RGO in lithium-ion batteries, J. Mater. Chem. A 1 (2013) 8658–8664.

[20] G.K. Veerasubramani, M.-S. Park, G. Nagaraju, D.-W. Kim, Unraveling the Na-ion storage performance of a vertically aligned interlayer-expanded two-dimensional MoS$_2$@C@MoS$_2$ heterostructure, J. Mater. Chem. A 7 (2019) 24557–24568.

[21] Q. Pan, F. Zheng, Y. Wu, X. Qu, C. Yang, X. Xiong, M. Liu, MoS$_2$-covered SnS nanosheets as anode material for lithium-ion batteries with high capacity and long cycle life, J. Mater. Chem. A 6 (2018) 592–598.

[22] J. Pei, H. Geng, E.H. Ang, L. Zhang, X. Cao, J. Zheng, H. Gu, Controlled synthesis of hollow C@TiO$_2$@MoS$_2$ hierarchical nanospheres for high-performance lithium-ion batteries, Nanoscale 10 (2018) 17327–17334.

[23] P. He, Y. Fang, X.Y. Yu, X.W.D. Lou, Hierarchical nanotubes constructed by carbon–coated ultrathin SnS nanosheets for fast capacitive sodium storage, Angew. Chem., Int. Ed. 56 (2017) 12202–12205.

[24] X. Hu, J. Chen, G. Zeng, J. Jia, P. Cai, G. Chai, Z. Wen, Robust 3D macroporous structures with SnS nanoparticles decorating nitrogen-doped carbon nanosheet networks for high performance sodium-ion batteries, J. Mater. Chem. A 5 (2017) 23460–23470.

[25] T. Zhou, W.K. Pang, C. Zhang, J. Yang, Z. Chen, H.K. Liu, Z. Guo, Enhanced sodium-ion battery performance by structural phase transition from two-dimensional hexagonal-SnS$_2$ to orthorhombic-SnS, ACS Nano 8 (2014) 8323.

[26] W. Wang, L. Shi, D. Lan, Q. Li, Improving cycle stability of SnS anode for sodium-ion batteries by limiting Sn agglomeration, J. Power Sources 377 (2018) 1–6.

[27] P. Xue, N. Wang, Y. Wang, Y. Zhang, Y. Liu, B. Tang, Z. Bai, S. Dou, Nanoconfined SnS in 3D interconnected macroporous carbon as durable anodes for lithium/sodium ion batteries, Carbon 134 (2018) 222–231.

[28] X. Ou, L. Cao, X. Liang, F. Zheng, H.S. Zheng, X. Yang, J.H. Wang, C. Yang, M. Liu, Fabrication of SnS$_2$ /Mn$_2$SnS$_4$ /Carbon heterostructures for sodium-ion batteries

[29] Y. Wang, J. Xu, H. Wu, M. Xu, Z. Peng, G. Zheng, Hierarchical SnO$_2$–Fe$_2$O$_3$ heterostructures as lithium-ion battery anodes, J. Mater. Chem. 22 (2012) 21923–21927.

[30] Y. Guo, J. Tang, H. Qian, Z. Wang, Y. Yamauchi, One-pot synthesis of zeolitic imidazolate framework 67-derived hollow Co$_3$S$_4$@MoS$_2$ heterostructures as efficient bifunctional catalysts, Chem. Mater. 29 (2017) 5566–5573.

[31] Y. Su, C. Wu, H. Li, F. Chen, Y. Guo, L. Yang, S. Xu, MoS$_2$ nanoplatelets scaffolded within CoS$_2$ nanobundles as anode nanomaterials for sodium-ion batteries, J. Alloy. Compd. 845 (2020) 1–7 156229.

[32] P. Liu, J. Han, K. Zhu, Z. Dong, L. Jiao, Heterostructure SnSe$_2$/ZnSe@PDA nanobox for stable and highly efficient sodium-ion storage, Adv. Energy Mater. 10 (2020) 1–8 2000741.

[33] X. Man, P. Liang, H. Shu, L. Zhang, D. Wang, D. Chao, Z. Liu, X. Du, H. Wan, H. Wang, Interface synergistic effect from layered metal sulfides of MoS$_2$/SnS$_2$ van der Waals heterojunction with enhanced Li-ion storage performance, J. Phys. Chem. C 122 (2018) 24600–24608.

[34] L. Cao, X. Gao, B. Zhang, X. Ou, J. Zhang, W.B. Luo, Bimetallic sulfide Sb$_2$S$_3$@FeS$_2$ hollow nanorods as high-performance anode materials for sodium-ion batteries, ACS Nano 14 (2020) 3610–3620.

[35] G.K. Veerasubramani, M.-S. Park, J.-Y. Choi, Y.-S. Lee, D.-W. Kim, Rational combination of an alabandite MnS laminated pyrrhotite Fe$_{1\_x}$S nanocomposite as a superior anode material for high performance sodium-ion battery, ACS Sustainable Chem. Eng. 7 (2019) 5921–5930.

[36] M. Chen, Z. Zhang, L. Si, R. Wang, J. Cai, Engineering of yolk–double shell cube-like SnS@N–S codoped carbon as a high-performance anode for Li- and Na-ion batteries, ACS Appl. Mater. Interfaces 11 (2019) 35050–35059.

[37] C. Wu, X. Tong, Y. Ai, D.S. Liu, P. Yu, J. Wu, Z.M. Wang, A Review, Enhanced anodes of Li/Na-ion batteries based on yolk–shell structured nanomaterials, Nano-Micro Lett 10 (2018) 1–18 40.

[38] Y. Yao, M.T. McDowell, I. Ryu, H. Wu, N. Liu, L. Hu, W.D. Nix, Y. Cui, Interconnected silicon hollow nanospheres for lithium-ion battery anodes with long cycle life, Nano Lett 11 (2011) 2949–2954.

[39] Y. Sun, X. Hu, J.-C. Yu, Q. Li, L. Yuan, W. Zhang, Y. Huang, Morphosynthesis of a hierarchical MoO$_2$ nanoarchitecture as a binder-free anode for lithium-ion batteries, Energy Environ. Sci. 4 (2011) 2870–2877.

[40] Y. Jiang, D. Song, J. Wu, Z. Wang, S. Huang, Y. Xu, Z. Chen, B. Zhao, J. Zhang, Sandwich-like SnS$_2$/Graphene/SnS$_2$ with expanded interlayer distance as high-rate Lithium/Sodium-ion battery anode materials, ACS Nano (2019) 9100–9111.

[41] K. Krishnamoorthy, G.K. Veerasubramani, P. Pazhamalai, S.-J. Kim, Designing two dimensional nanoarchitectured MoS$_2$ sheets grown on Mo foil as a binder free electrode for supercapacitors, Electrochim. Acta 190 (2016) 305–312.

[42] J. Xia, L. Liu, S. Jamil, J. Xie, H. Yan, Y. Yuan, Y. Zhang, S. Nie, J. Pan, X. Wang, G. Cao, Free-standing SnS/C nanofiber anodes for ultralong cycle-life lithium-ion batteries and sodium-ion batteries, Energy Storage Mater 17 (2019) 1–11.

[43] G.H. Yue, Y.D. Lin, X. Wen, L.S. Wang, Y.Z. Chen, D.L. Peng, Synthesis and characterization of the SnS nanowires via chemical vapor deposition, Appl. Phys. A 106 (2012) 87–91.

[44] F.-H. Zheng, Q.-C. Pan, C.-H. Yang, X.-H. Xiong, X. Ou, R.-Z. Hu, Y. Chen, M.L. Liu, Sn-MoS$_2$-C@C microspheres as a sodium-ion battery anode material with high capacity and long cycle life, Chem.–Eur. J 23 (2017) 5051–5058.

[45] Q.-C. Pan, F.-H. Zhang, Y.-N. Wu, X. Ou, C.-H. Yang, X.-H. Xiong, M.-L. Liu, MoS$_2$-covered SnS nanosheets as anode material for lithium-ion batteries with high capacity and long cycle life, J. Mater. Chem. A 6 (2018) 592–598.

[46] P. Ge, H. Hou, S. Li, L. Yang, X. Ji, Tailoring rod-like FeSe$_2$ coated with nitrogen–doped carbon for high-performance sodium storage, Adv. Funct. Mater. 28 (2018) 1–12 1801765.

[47] B. Jiang, Y. He, B. Li, S. Zhao, S. Wang, Y.B. He, Z. Lin, Polymer-templated formation of polydopamine-coated SnO$_2$ nanocrystals: Anodes for cyclable lithium-ion batteries, Angew. Chem., Int. Ed. 56 (2017) 1869–1872.

[48] Q.C. Pan, F.H. Zhang, Y.N. Wu, X. Ou, C.H. Yang, X.H. Xiong, M.L. Liu, MoS$_2$-covered SnS nanosheets as anode material for lithium-ion batteries with high capacity and long cycle life, J. Mater. Chem. A 6 (2018) 592–598.

[49] Q.Y. Li, Q.C. Pan, G.H. Yang, X.L. Lin, Z.X. Yan, H.Q. Wang, Y.G. Huang, Synthesis of Sn/MoS$_2$/C composites as high-performance anodes for lithium-ion batteries, J. Mater. Chem. A 3 (2015) 20375–20381.

[50] Y. Du, Z. Yin, X. Rui, Z. Zeng, X.J. Wu, J. Liu, Y. Zhu, J. Zhu, X. Huang, Q. Yan, H. Zhang, facile, relative green, and inexpensive synthetic approach toward large-scale production of SnS$_2$ nanoplates for high-performance lithium-ion batteries, Nanoscale 5 (2013) 1456–1459.

[51] S.H. Choi, Y.C. Kang, Aerosol-assisted rapid synthesis of SnS-C composite microspheres as anode material for Na-ion batteries, Nano Res 8 (2015) 1595.

[52] J. Qiu, Z. Zhang, Q. Li, Y. Li, X. Wu, C. Qi, Q. Qian, Formation of N-doped molybdenum carbide confined in hierarchical and hollow carbon nitride microspheres with enhanced sodium storage properties, J. Mater. Chem. A 4 (2016) 13296–13306.

[53] J. Shi, Y. Wang, Q. Su, F. Cheng, X. Kong, J. Lin, T. Zhu, S. Liang, A. Pan, N-S co-doped C@SnS nanoflakes/graphene composite as advanced anode for sodium-ion batteries, Chem. Eng. J. 353 (2018) 606–614.

[54] Y. Li, H. Wang, B. Huang, L. Wang, R. Wang, B. He, Y. Gong, X. Hu, Mo$_2$C-induced solid-phase synthesis of ultrathin MoS$_2$ nanosheet arrays on bagasse-derived porous carbon frameworks for high-energy hybrid sodium-ion capacitors, J. Mater. Chem. A 6 (2018) 14742–14751.

[55] X. Xiong, C. Yang, G. Wang, Y. Lin, X. Ou, J.-H. Wang, B. Zhao, M. Liu, Z. Lin, K. Huang, SnS nanoparticles electrostatically anchored on three-dimensional N– doped graphene as an active and durable anode for sodium-ion batteries, Energy Environ. Sci. 10 (2017) 1757.

[56] Z.-T. Shi, W. Kang, J. Xu, Y.-W. Sun, M. Jiang, T.-W. Ng, H.-T. Xue, D.Y.W. Yu, W. Zhang, C.-S. Lee, Hierarchical nanotubes assembled from MoS$_2$-carbon monolayer sandwiched superstructure nanosheets for high-performance sodium ion batteries, Nano Energy 22 (2016) 27–37.

[57] G. Fang, Z. Wu, J. Zhou, C. Zhu, X. Cao, T. Lin, Y. Chen, C. Wang, A. Pan, S. Liang, Observation of Pseudocapacitive Effect and Fast Ion Diffusion in Bimetallic Sulfides as an Advanced Sodium-Ion Battery Anode, Adv. Energy Mater. 8 (2018) 1–10 1703155.

[58] T. Brezesinski, J. Wang, S.-H. Tolbert, B. Dunn, Ordered mesoporous α-MoO$_3$ with iso-oriented nanocrystalline walls for thin-film pseudocapacitors, Nat. Mater. 9 (2010) 146–151.